

Studies of a Laser-Produced Carbon Plasma with Spatial, Temporal and Spectral Resolution

Diploma paper
by
Claire Lyngå

Lund Reports on Atomic Physics, LRAP-164
Lund, July 1994

This thesis was submitted to the
Faculty of Technology at the
University of Lund
in partial fulfilment of the requirements
for the degree of Master of Science

Abstract

A study of a laser-produced carbon plasma is presented. Plasmas were produced by focusing a Q-switched Nd:YAG laser beam onto a plane target. Spatial, temporal and spectral resolution was obtained with two detection systems; a multi-colour imaging system producing two-dimensional images of the expanding plasma and a monochromator allowing for spectral studies. Three ion species; CII, CIII and CIV were mainly investigated. Some results concerning atomic carbon, CI, have been included. Studies of the expanding plume shapes, ion velocities and time of appearance are presented. Results show that the more highly ionized species have a higher ion velocity, a smaller spread as they expand and appear earlier than the less ionized species. Spectroscopic studies at different distances from the target were performed. Assuming that the local thermal equilibrium (LTE) model is applicable, electron temperatures in different parts of the plasma have been calculated using these spectra.

Contents

1	Introduction	1
2	Basic properties of a plasma	
2.1	Parameters describing the plasma	2
2.2	Plasma oscillation	2
2.3	Recombination processes	3
2.4	Emission processes in a plasma	4
3	Plasma models	
3.1	Coronal equilibrium	5
3.2	Local thermal equilibrium	5
3.3	Collisional-radiative equilibrium	6
3.4	Plasma formation and expansion	7
3.5	The self regulating plasma model	8
4	Experimental arrangement	
4.1	The multi-colour imaging system	10
4.2	Spectrally resolved measurements	12
5	Space and time resolved emission studies	
5.1	Images of the plasma	13
5.2	Spectroscopic studies of the plasma	19
5.3	Calculation of electron temperatures	22
5.4	Conclusion	23
	Acknowledgements	24
	References	25
	Appendix A - Table of carbon spectral lines	27
	Appendix B - Carbon spectra	28

1 Introduction

Pulsed high-power lasers have opened new possibilities for generating plasmas. Plasmas with very high density and temperature are produced by concentrating the laser radiation on the surface of a solid target. Laser ablation and laser produced plasmas are of interest for a number of applications, including the production of new laser sources [1], the production of VUV radiation [2], as an intense source of radiation in the soft x-ray region and the production of atomic species of low vapour pressure for spectroscopy [3]. At the Lund High Power Laser Laboratory, laser-produced plasmas are used especially in work with time-resolved spectroscopy [4] and as a source for high-order harmonic generation [5]. For these projects it is of interest to investigate the formation and expansion of the different ion species in the plasma. The desired result may be a clear spatial and temporal separation of the ion species. When time-resolved spectroscopy is considered the ion distribution at distances of approximately 1 cm from the target are the most interesting. For work with harmonic generation distances of about 1 mm are relevant.

In this diploma thesis a spatial, temporal and spectral study of a laser-produced plasma is presented. By focusing a Q-switched Nd:YAG laser beam onto a carbon target, plasmas were produced. A two-dimensional image of the expansion of different ion species was obtained with interference filters using a special imaging arrangement. Spectral measurements were done to supplement these studies. A carbon target was chosen since its spectrum is relatively uncomplicated in the visible region.

This thesis is divided into five chapters. Following this chapter, a short theory of the basic properties of a laser-produced plasma is presented. Chapter 3 deals with different plasma models relevant for this project. The experimental method and equipment used is treated in Chapter 4. Chapter 5 is comprised of a presentation and discussion of the results. A table of spectral lines of carbon in the visible region are included in Appendix A and recordings of the carbon spectra can be found in Appendix B.

2 Basic properties of a plasma

2.1 Parameters describing the plasma

A plasma consists of electrons, ions and in some cases excited atoms and molecules. Due to charge neutrality the number of free electrons in the plasma, n_e , must be equal to the number of emitted electrons from the ions. In the plasma as a whole this condition is always fulfilled. For a smaller system this condition requires that the characteristic length of the system is much larger than the *Debye length*, λ_D . The Debye length is defined by

$$\lambda_D = \sqrt{\frac{kT_e}{4\pi n e^2}} \quad (2.1)$$

Here n is the plasma density ($n=n_e$), e is the electron charge and T_e the electron temperature. The electron temperature is the kinetic energy of the electrons expressed in terms of kT_e , where k is the Boltzmann constant. A physical understanding of the Debye length can be gained by considering a charged particle inserted into the plasma. The Coulomb potential induces an electric polarization since it attracts (or repels) the charge of opposite (or same) sign. This polarization charge cancels the charge of the inserted particle and thereby restricts the effective range of the Coulomb potential. This phenomenon is known as *Debye shielding* and the Debye length is the distance at which this shielding is almost complete.

2.2 Plasma oscillation

The particle density in a plasma displays certain fluctuations. If the electron density at one point increases relative to the ion density, Coulomb forces will pull the electrons back to their original positions. Because of their inertia, however, the electrons overshoot their original positions and must reverse again. This oscillation about the equilibrium position takes place at a characteristic angular *electron plasma frequency* (ω_{pe}) given by

$$\omega_{pe} = \sqrt{\frac{n_e e^2}{m_e \epsilon_0}} \quad (2.2)$$

A corresponding ion plasma oscillation is produced as a response to the electron oscillation. However, because of the large mass of the ion, this oscillation can be neglected.

The extent of the fluctuations is approximately equal to the Debye length. We can therefore estimate the mean velocity of the electrons as

$$\omega_{pe}\lambda_D = \sqrt{\frac{kT_e}{m_e}} \quad (2.3)$$

When the frequency of the incident plasma-generating light is equal to the plasma frequency we get the corresponding *critical electron density*, n_{ec} .

$$n_{ec} = \omega_{pe}^2 \frac{m_e \epsilon_0}{e^2} \quad (2.4)$$

The permittivity of vacuum is ϵ_0 . For $n_e > n_{ec}$ there is a strong reflection of the incoming light. Absorption is strongest in plasma with a density less than but close to n_{ec} [6]. The reflectivity is very sensitive to the gradient of the electron density. If the density initially rises rapidly and then slowly approaches n_{ec} , the absorption will be greater than in the case of a linear variation over the same distance [7]. For neodymium laser light ($\lambda=1.06 \mu\text{m}$), n_{ec} is $\sim 10^{21} \text{ cm}^{-3}$.

2.3 Recombination processes

The following recombination processes are possible between positive ions and electrons:

Radiative recombination



Dielectronic recombination



Three-body recombination



Here A^* and A^{**} denotes the singly and doubly excited atom, respectively. The degree of ionization is z .

In *radiative recombination* a free electron is captured by a z -times ionized atom and makes a transition to a bound state of the $(z-1)$ -times ionized atom. The surplus energy is emitted as a photon.

In *dielectronic recombination* a free electron may be captured, without the emission of radiation, into a higher energy level of the ion. Instead of the emitted radiation, one of

the bound electrons is excited to a higher level by the excess energy. The now doubly excited atom or ion is de-excited by photon emission or through an inelastic collision. The rate of this process is known to be very small [8].

Three-body recombination may occur if two electrons collide with the ion simultaneously. One electron is captured into an upper excited level and the other electron carries away the surplus energy. The captured electron cascades down to the ground state either by radiative transitions or collisions. Three-body recombination is in competition with radiative recombination and becomes more probable as the density increases [7].

2.4 Emission processes in a plasma

The emitted radiation in a plasma is due to three different mechanisms. One distinguishes between Bremsstrahlung, recombination radiation and line radiation.

Bremsstrahlung. This is also called free-free radiation and is emitted when a free electron is decelerated in the field of another particle. A photon corresponding to the change in energy is emitted, giving rise to a continuous spectrum. In a hot plasma electron-ion collisions are the most important mechanisms for Bremsstrahlung, while in a slightly ionized gas, collisions between electrons and neutral atoms are more important. Electron-electron collisions emit radiation only at relativistic velocities. Bremsstrahlung is the dominant radiation mechanism for plasmas hot enough for most of the ions to be stripped of all their orbital electrons.

Recombination radiation. This process which has already been mentioned in Section 2.3 is also known as free-bound radiation. It occurs when a free electron is captured into a bound state, emitting a photon corresponding to the initial kinetic energy plus the ionization energy of the bound state. The spectrum will therefore be a continuum with a sharp low-frequency cut-off.

Line radiation. Transitions between discrete bound states result in line radiation, or bound-bound radiation as it is also called. The energy of the photon is well defined, resulting in a discrete spectral line. The width of the line depends on the spontaneous lifetime of the upper state, and on the velocity distribution of the atoms (Doppler shifts). Collisions, electric and magnetic fields also affect the line profile. A complication may arise if the emitted light interacts with other particles before being detected. Often the plasma is assumed to be optically thin, which means that the photons escape without being reabsorbed.

3 Plasma models

The emission spectrum of a laser plasma depends on the combined effects of many processes such as radiative and collisional excitation, de-excitation, ionization and recombination. Often many energy levels and ionization stages are involved. The emission spectrum could in principle be predicted if the rates of all these processes were known. However, because of the complexity of the problem, simplified models of the plasma are used.

Three different plasma models are considered below. A Maxwellian distribution of the free electrons is assumed throughout. Hence, at a certain electron temperature T_e the number of electrons n_e with speeds between v and $v+dv$ is given by

$$dn_e(v) = 4\pi n_e \left(\frac{m_e}{2\pi k T_e} \right)^{3/2} \exp\left(\frac{-m_e v^2}{2k T_e} \right) v^2 dv \quad (3.1)$$

3.1 Coronal equilibrium

In low density plasmas collisional processes become less likely. An excited atom will therefore generally have time to radiate a photon before being de-excited by a collision. Assuming that the plasma is optically thin, excitation by absorption of the photons emitted in the plasma is unlikely. This means that in equilibrium a balance occurs between collisional excitation and spontaneous radiative de-excitation. Nearly all atoms and ions are in their ground states, with radiative decay from the upper levels to the lower levels, balanced by collisional excitation. In the same way collisional ionization is balanced by radiative recombination in the coronal model. Since both these processes are proportional to the electron density, the amounts of the different ionic charge states are independent of the electron density.

The validity of the model is restricted to sufficiently low electron densities, where collisional transitions from an excited level are slower than radiative emission. However, as the principal quantum number n increases, the probability of collisional processes increases, but the probability of spontaneous radiation falls. This leads to a breakdown of the coronal model for high n .

3.2 Local thermal equilibrium (LTE)

As the density of the plasma increases collisions become more frequent. At sufficiently high densities the population of the excited states will be determined by collisions rather than radiative processes. In the LTE model it is assumed that the population is controlled entirely by collisions.

The populations of two bound states 1 and 2 of an atom or ion are then related by the Boltzmann equation, where g_1 and g_2 are the statistical weights, and E_1 and E_2 the energies of the two states:

$$\frac{n_1}{n_2} = \frac{g_1}{g_2} \exp\left(\frac{E_2 - E_1}{kT_e}\right) \quad (3.2)$$

The densities n_z of ground state atoms ($z = 0$) or ions ($z = 1, 2, \dots$) are related by Saha's equation:

$$\frac{n_e n_{z+1}}{n_z} = \frac{2(g_0)_{z+1}}{(g_0)_z} \left(\frac{2\pi m_e kT_e}{h^2}\right)^{3/2} \exp\left(-\frac{\chi_z}{kT_e}\right) \quad (3.3)$$

The statistical weight of the ground state of an atom or ion of charge Z , is $(g_0)_z$ and χ_z is its ionization energy. By combining the equation for all adjacent stages of ionization, together with the total density of nuclei, the ionization equilibrium potential can be completely determined. For the LTE model to apply the collisional de-excitation must be approximately ten times more probable than radiative decay. This corresponds, in an optically thin plasma, to the requirement that

$$n_e \geq 1.73 \cdot 10^{14} T_e^{1/2} (\Delta\omega)_{\max}^3 \quad (3.4)$$

where $(\Delta\omega)_{\max}$ is the largest distance between adjacent energy levels given in eV. The unit of n_e is in cm^{-3} and T_e in eV [9]. This may be a large fraction of the ionization potential of the species present in the plasma. Laser produced plasmas are in LTE soon after formation because the electron density is large, but the plasmas lose equilibrium as they expand [6].

3.3 Collisional-radiative equilibrium

The above models are valid at either high or low electron densities. The collisional-radiative model covers the intermediate region. It is a modification of the coronal model taking into account collisional transitions from higher bound levels as well as radiative decay, and three-body recombination as well as radiative recombination. A detailed description of the model can be found in *Bates et al.* [10,11].

3.4 Plasma formation and expansion

The processes involved in plasma production are complex. Heating of the target, melting, vaporization and ionization must be taken into consideration. The geometry of the target and the laser beam, as well as the time dependence of the laser pulse, determines the plasma dynamics. The impact of the light varies from only a rise in temperature at low irradiances, to multi-photon ionization at high irradiances.

Thermal conductivity. When the laser light hits the target, part of it is reflected and the rest is normally absorbed by electrons which are raised to a higher state. Energy is then transferred by collisions and radiative processes to the rest of the solid. Provided the laser light is approximately constant for longer than the relaxation times of the electrons (in the order of 10^{-12} to 10^{-13} seconds) an equilibrium is reached and a temperature may be defined at every point.

Melting and vaporization. The next stage in the plasma production is when the target temperature reaches the melting point. In most cases this liquid phase is not very significant. The energy required is small compared with the vaporization or ionization energy. Once the boiling point is reached vaporization occurs. At low irradiances the rate of evaporation is small and the vapour layer will not absorb light effectively. As the irradiance increases the initial rate of evaporation will increase and more light will be absorbed.

Ionization. The vapour, generated by the laser pulse, may reach a temperature high enough for the atoms to undergo thermal ionization, i.e. the atoms or ions are ionized by collisions. Provided the vapour is sufficiently dense for thermodynamic equilibrium to be maintained, the population densities can be related by Saha's equation (Eq. 3.3). The main process for energy transfer from the laser field to the electrons is by *inverse Bremsstrahlung*. Here an electron moves from one free state to a more energetic one by the absorption of a photon according to Eq. 3.5.



The absorption coefficient for this process is:

$$\kappa_{\omega} = 5.64 \cdot 10^{-11} \frac{Z n_e^2 \ln \Lambda}{\omega^2 T_e^{3/2}} * \frac{1}{\left(1 - \frac{\omega_{pe}^2}{\omega^2}\right)^{1/2}} \quad (3.6)$$

The frequency of the laser light is ω . T_e , n_e and Z are as defined earlier. The plasma frequency, ω_{pe} , is given by Eq. 2.2. Λ is a factor related to the electron-ion collisions. For laser-produced plasmas $\ln \Lambda$ takes on a value between 5 and 10 [12]. At the beginning of plasma formation $\omega \gg \omega_{pe}$, making the second factor in Eq. 3.6 close to unity. The rate of absorption then depends mainly on n_e^2 . As more energy is absorbed the ionization process continues. Consequently, n_e approaches n_{cc} and the surface of the plasma becomes opaque to the incoming laser light.

At very high irradiances *multi-photon ionization* takes place during a few cycles of the electric field. In this process the atom or ion will emit an electron by absorbing more than one photon.

3.5 The self regulating plasma model

For a pulse lasting several nanoseconds and focused onto a small diameter the *self regulating plasma model* for laser heating is appropriate. Here, the plasma closest to the target will always be dense and therefore attenuate the incoming light. As the plasma expands the outer layer becomes less dense and will absorb less light. This means that more light reaches the target, increasing the vaporization rate and plasma density. In the same way an increased density in the outer layer will reduce the amount of light that reaches the target and thereby decrease the plasma density. A steady-state will be reached if the duration of the laser pulse is longer than the time which an electron-ion pair spends within the zone of heating. In the case of nanosecond pulses this condition is generally fulfilled [13].

Puell [13] considered a model where the plasma was divided into three separate regions. A figure of the interaction region is shown below in figure 3.1.

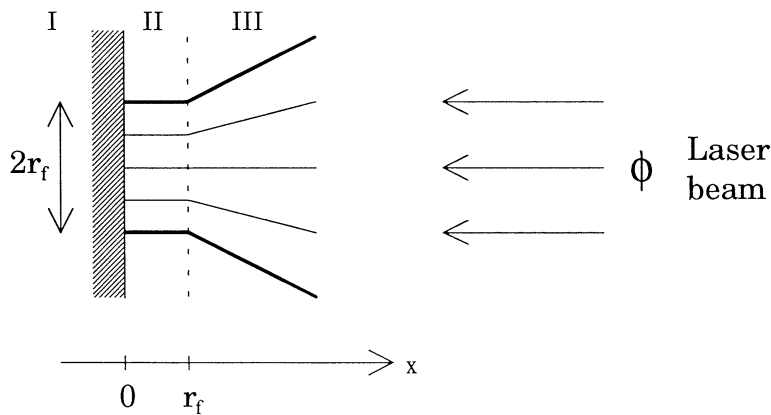


Fig. 3.1. Schematic drawing of plasma flow from target during laser heating.

Region I ($x < 0$) is comprised of the undisturbed target. The boundary between regions II and III is a distance from the target which is equal to the radius of the focal spot (r_f). In region II ($0 < x < r_f$) the plasma is assumed to be very dense and expanding in only one direction. Three-dimensional flow occurs in region III ($x > r_f$). Because of the spatial flow in region III there is a rapid decrease of density. This means that most of the heating occurs in region II where the density is higher. This region is therefore called the *heating zone* and is the main region of interest. Because of conservation of

momentum a shock wave will penetrate region I. However, the energy transfer in this process may be neglected since the densities of the target and the plasma differ significantly.

In the heating zone inverse Bremsstrahlung is the dominant mechanism for transferring energy from the laser field to the electrons. Once the electrons have been heated they transfer energy to the ions. In the heating zone the density is high enough for the electrons to transfer energy to the ions more rapidly than they are heated. Therefore the electron and ion temperature is equal. Outside the heating zone random thermal energy is transferred to directed kinetic energy (the plasma expands). During the expansion $T_e \neq T_{ion}$ because of the rapid decrease of plasma density. The time is too short for an equilibrium to be attained. Puell found expressions for the ion and electron temperatures at the boundary between regions II and III. The plasma temperature, $T_{e,max}$, which is the maximum temperature achieved anywhere in the plasma is given by

$$kT_{e,max} = \xi^{-2/3} \left(\frac{3m_i \psi r_f}{50} \right)^{2/9} \Phi^{4/9} \quad (3.7)$$

The parameter ψ is equal to $2.5 \cdot 10^{-55} \cdot (\omega_{ruby}/\omega_0)$, ω_{ruby} being the frequency of the ruby laser used in the study, and ω_0 that of the laser light. ξ is a factor compensating for the fact that T_e might not be equal to T_{ion} , as predicted in the model. Depending on the ratio T_{ion}/T_e , ξ varies from 1 when $T_{ion} = 0$, to $(Z+1)/Z$, when $T_{ion} = T_e$. The irradiance of the incoming light is Φ , and the ion mass is m_i .

4 Experimental Arrangement

Plasmas were produced by focusing a Q-switched Nd:YAG laser beam onto a plane target. The beam was focused with a 25 cm focal length lens, onto the target surface, at normal incidence. Depending on laser intensity, and the position of the target relative to the beam waist, intensities of 10^9 - 10^{11} W/cm² were obtained. The Nd:YAG laser emits light in the infra-red region with a wavelength of 1.06 μ m. The target was situated in a chamber with a vacuum of approximately 10^{-5} mbar and was rotated so as to ablate a fresh surface.

Two different detection systems were used to study the plasma. The major part of the project used the set-up described in Section 4.1. Here an image of the plasma was obtained using a multi-colour imaging system [14,15,16]. To supplement the imaging measurements, spectra of the plasma were recorded using the arrangement described in Section 4.2.

4.1 The multi-colour imaging system

The plasma light was collected by a Cassegrainian telescope, via a system of lenses. This specially designed telescope has its primary mirror split into four parts, each somewhat tilted (see Fig. 4.1). Each mirror segment will produce an image of the object at a small distance off the optical axis, so that four identical but separated images are obtained.

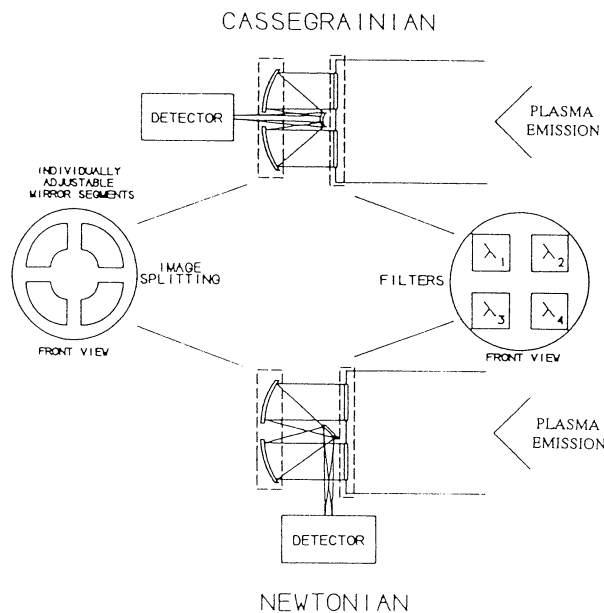


Fig. 4.1. Cassegrainian and Newtonian reflective optics systems. The upper arrangement was used for plasma emission studies. Adapted from [15].

By placing bandpass filters in front of the Cassegrainian mirror segments four different spectral lines can be observed simultaneously. An appropriate choice of bandpass

filters will thus enable us to view up to four different ionization stages in the original image. The four filtered images were placed in four quadrants adjacent to each other on an image intensifier. We used a gated Delli-Delti CP1/NS2 microchannel plate image intensifier with a S20R spectral response. The microchannel plate (MCP) was gated by switching the potential, which was approximately 200 V, between the photocathode and the MCP. The voltage over the MCP was about 10 kV and could be varied in order to change the amplification.

With two lenses of focal length 27 mm and 25 mm, the image was projected onto a CCD camera. Trigger signals from a Stanford Research System SRS535 delay unit enabled exact synchronization of the image intensifier with the laser pulse. The image intensifier was gated down to 25 ns. The gate was moved out in the time domain allowing the temporal development of the plasma to be studied. The signal from a photodiode directed towards the laser beam, together with a signal synchronous with the temporal detection window, was viewed on a digital oscilloscope so that the time at which the image was captured could be related to the time of plasma formation. The video signal from the CCD camera was monitored on a 486 compatible personal computer. The images were plotted in false colour on a colour printer. The arrangement is shown in Fig. 4.2, below.

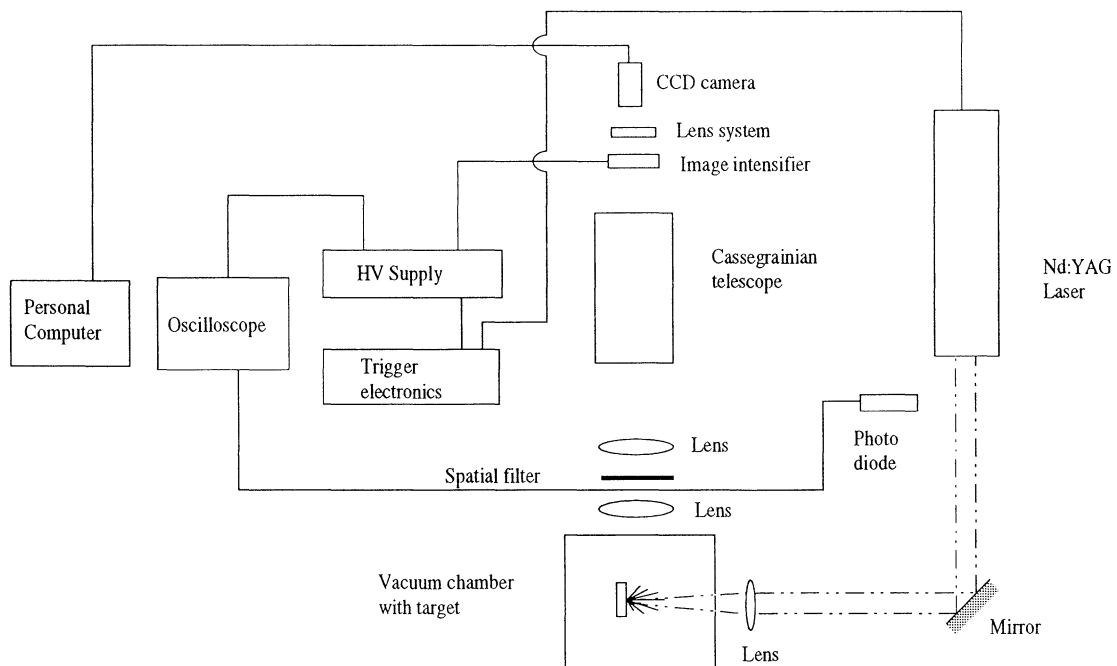


Fig. 4.2. Experimental set-up used for imaging studies.

The set-up described above was later modified by the removal of the Cassegrainian telescope. Although only allowing us to view one ion species at a time, a larger region of the plasma could be studied, since the problem of the images interfering with each other was avoided. The appropriate bandpass filter was now placed immediately in front of the image intensifier and the detection system moved closer to the vacuum chamber.

4.2 Spectrally resolved measurements

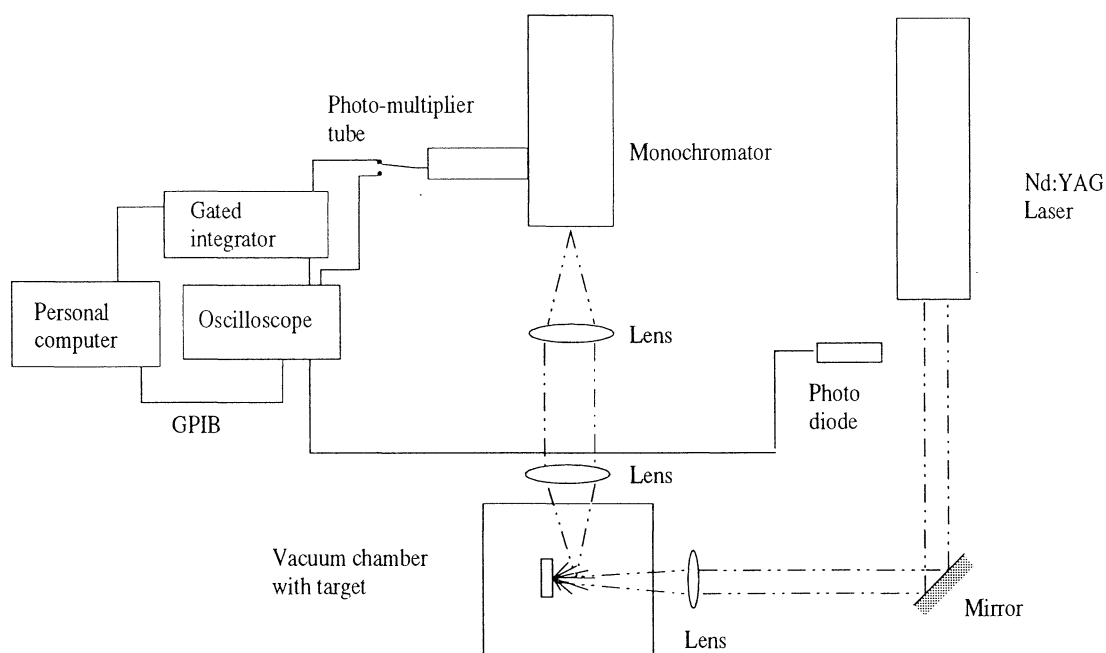


Fig. 4.3. Experimental set-up used for spectrally resolved studies.

The experimental set-up for the spectrally resolved measurements is shown in Fig. 4.3. The emitted plasma radiation was focused onto the entrance slit of a monochromator with a 1:1 imaging relation. Both the entrance and exit slits had widths of 1.5 mm. This gave adequate resolution while still collecting enough plasma light. A Hamamatsu R331 photomultiplier tube attached to the exit slit detected the signal. A Stanford Research 265 gated integrator was used to improve the signal. By moving the time window out in the temporal domain a spectrum was obtained at a chosen time after the laser ablation. Spectra up to 400 ns after ablation were studied. The target was translated in the direction parallel to the incoming laser light. This enabled us to study changes in the spectra at increasing distances from the target. Spectra ranging from 400 to 600 nm were scanned at distances from the target of up to 30 mm.

Measurements were also taken with the monochromator kept at a constant wavelength. This allowed us to study the variation in intensity of one spectral line with respect to time. The signal was displayed on a digital storage oscilloscope and transferred to a PC with a GPIB interface.

5 Space and time resolved emission studies

5.1 Images of the plasma

A scan of the spectrum from 400 nm to 600 nm (see figure 5.1) was obtained using the set-up described in Section 4.2. At 500 nm, the voltage over the photomultiplier was raised, increasing the sensitivity by a factor 8.

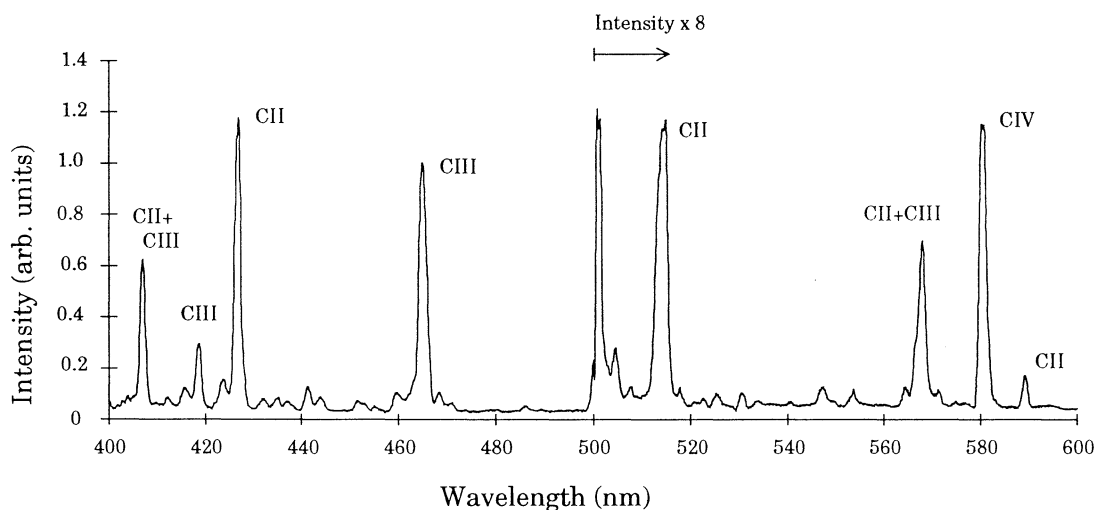


Fig. 5.1. Carbon spectrum, 10 mm from the target, at 50 ns after plasma formation.

By using the Cassegrainian telescope in the set-up described in Section 4.1 images of the plasma were obtained. The transitions and interference filters used are listed below in Table 5.1. The spectral lines of CII and CIII are considerably stronger than the one for CIV.

Ion	Transition	Wavelength (nm)	Interference filter (nm)
CII	$3d(^2D_{3/2,5/2})-4f(^2F_{5/2,7/2})$	426.7	421 ± 5
CIII	$2s3s(^3S_1)-2s3p(^3P_{0,1,2})$	464.9	470.5 ± 4.5
CIII	$2p3s(^3P_{0,1,2})-2p3p(^3D_{1,2,3})$	466.3	
CIV	$3s(^2S_{1/2})-3p(^2P_{1/2,3/2})$	580.5	580 ± 4.5

Table 5.1. Transitions and interference filters used for imaging studies.

Attempts were made to use other transitions, CIII: 416.4 nm, 418.8 nm and CII: 514.2 nm. However, the intensity of these lines was found to be too low. No suitable lines were found for CI. Instead this fourth image was used as a reference to study the influence of the continuous emission in the images. An interference filter at 540 nm ($\Delta\lambda=8$ nm) was used. This region was chosen since it was relatively free from spectral lines.

For the discussion of the distribution of different ionic species in the plasma, the ionic charge will be referred to as the one in which the studied bound-bound transition occurs. When we are observing a z-times ionized atom, we might actually be studying a (z+1)-times ionized atom which has just recombined with an electron. Depending on the electron density and electron temperature, the energy state of the ion (z) which we observe is in thermal equilibrium with the ground state of the higher ion species (z+1). Therefore the emission spectrum might be strongly influenced by the presence of other ions.

In Fig. 5.2a-f a typical set of images is shown. Both the time interval between the shots and the exposure time is 25 ns. The laser output is 130 mJ/pulse, which produces an irradiance of the order of 10^{11} W/cm². The gain of the image intensifier has been increased as we move further out in time, as can be seen by the amplification factor. This factor has been scaled to unity at t=0 for the different ions. A dense plasma appears instantaneously when the laser hits the target. This will hereafter be referred to as the "spark". It emits continuous radiation, presumably due to the large amount of Bremsstrahlung present, since the plasma spark is very hot and most of the ions are stripped of their electrons. Because the spark is very intense compared to the emissions further out from the target we screened it off with a triangular piece of cardboard. The cardboard was placed in the image plane between the two lenses in front of the telescope. The spark appears far out in the time region on the pictures. We have assumed that this is because the voltage over the MCP, in the image intensifier, is not exactly zero outside the time window. If the emitted plasma light is intense enough, amplification may occur even outside the gated time region.

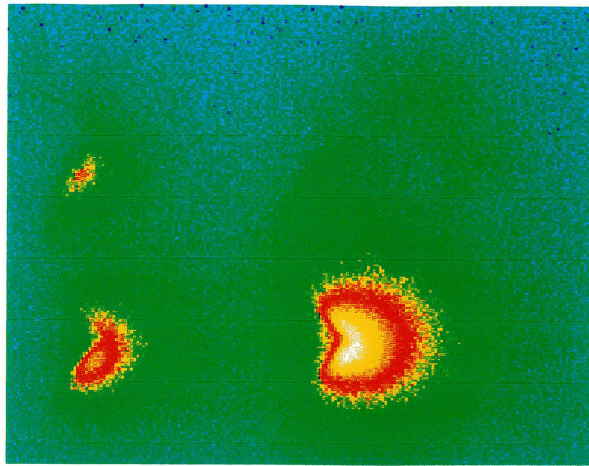
The first ion species to start to expand is CIII. It is followed by CII which starts to expand at approximately t=75 ns. CIV can only be seen faintly since this line is considerably weaker than the two others. Moving out in the time domain, the species expand, and it becomes hard to distinguish the four images from each other. As we tried to separate the four images further, the images were impaired by distortion between the image intensifier and the camera.

So as to be able to view a larger part of the plasma, the Cassegrainian telescope was removed, and one ionization stage studied at a time. The piece of cardboard was now placed immediately in front of the image intensifier. The irradiance was kept at $\sim 10^{11}$ W/cm², and the exposure time and time interval between pictures was 25 ns, except for CII where the time interval was larger. Results can be seen in Fig. 5.3-5.5. The shapes differ between the different ion species, the expanding plasma becoming narrower for the higher ions. CII has an oval shape, CIII has a more rounded shape, whereas the shape of CIV is more conical. CIII and CIV appear at approximately the same time and have similar expansion velocities. CII appears later and has a lower expansion velocity. The intensity of the signal of CII decreases at a slower rate than

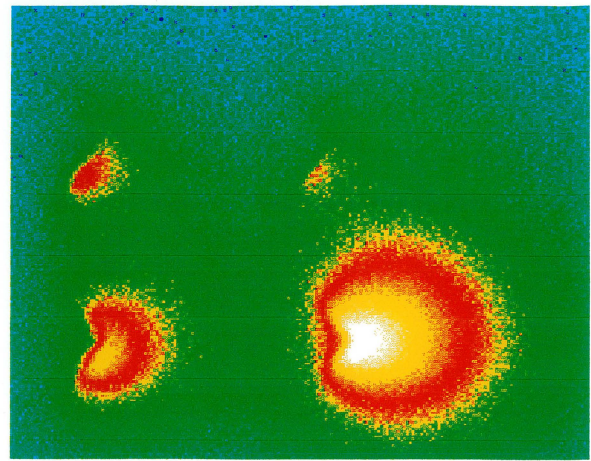
that of the two other ions. The expansion of CII is therefore followed further out in the time domain. CII and CIII disappear by loss of intensity as we follow the ions out from the target. CIV, although losing intensity markedly, seems to expand more distinctly and move out of the imaged region.

A disadvantage with the single colour images is that we cannot be sure that the same conditions prevail for the different images. One factor that influences the shape of the plume is a track made on the target. To prevent this from happening the laser beam was moved from time to time and a fresh surface was ablated. An extreme case where the laser beam hits a deep track is shown in Fig. 5.6. Two plasma plumes expand, from either side of the incoming laser light, in the direction of the track. Using the Cassegrainian telescope, now moved further away from the vacuum chamber, we obtained images that were smaller and better separated. From these, the shapes of CII and CIII could be confirmed (See Fig. 5.7a-b).

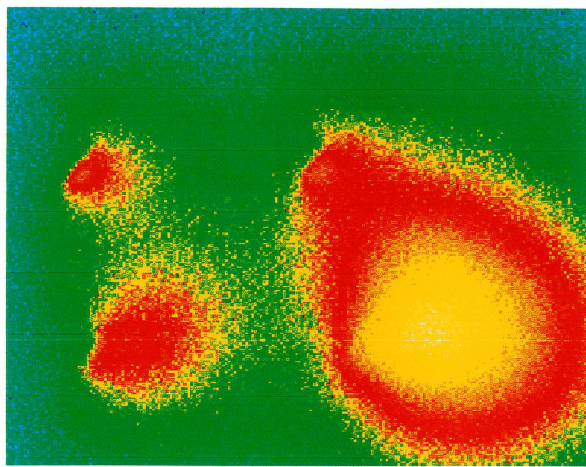
By changing the laser output from 40 mJ/pulse to 300 mJ/pulse we studied the effects of the irradiance on the produced plasma. This energy range corresponds to irradiances of 10^{10} - 10^{11} W/cm². The images produced were very similar in both temporal and spatial development. Different irradiances were also obtained by changing the position of the beam waist relative to the target. Irradiances of 10^9 - 10^{11} W/cm² were produced. Only the plasma produced with the lowest irradiance differed significantly. A small amount of CII was formed but there was no trace of CIII and CIV, as can be seen in Fig. 5.8.



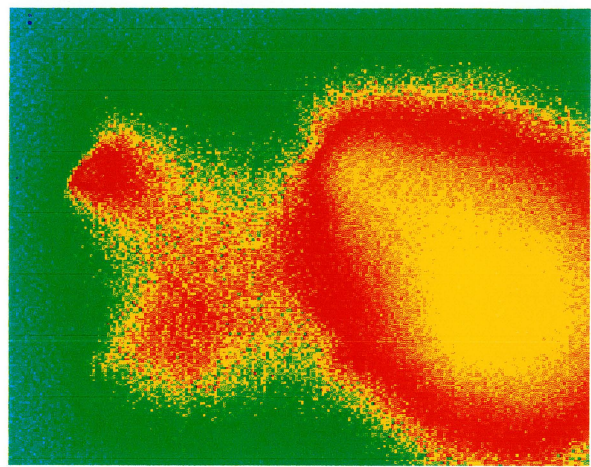
a) $t=0$ ns, Amplification=1.0



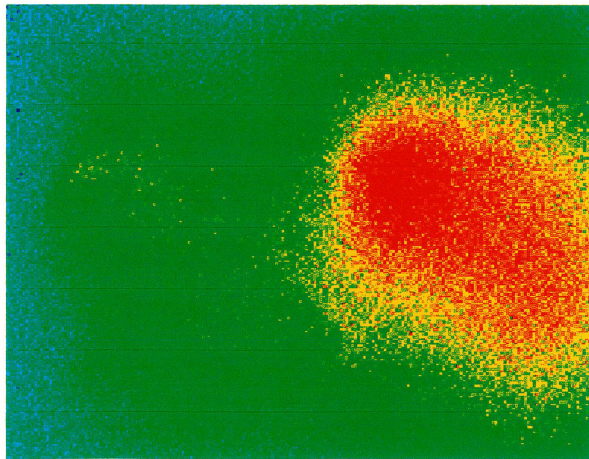
b) $t=25$ ns, Amplification=1.5



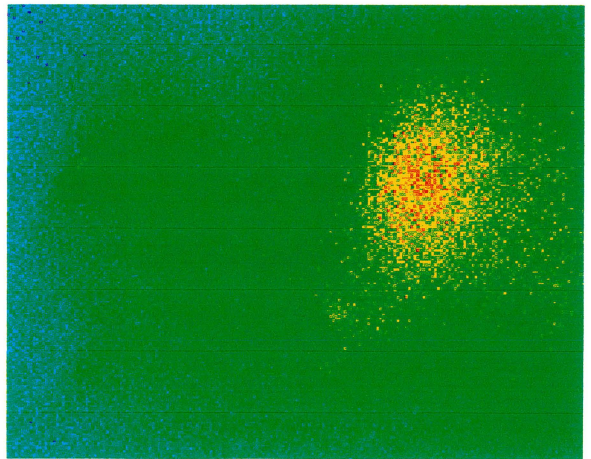
c) $t=50$ ns, Amplification=3.5



d) $t=75$ ns, Amplification=4.5



e) $t=100$ ns, Amplification=4.5

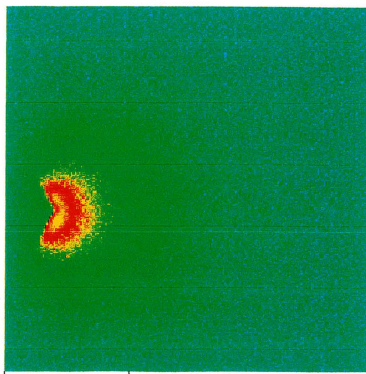


f) $t=125$ ns, Amplification=4.5

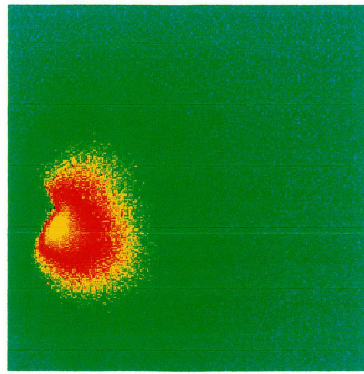


ref.	CII
CIV	CIII

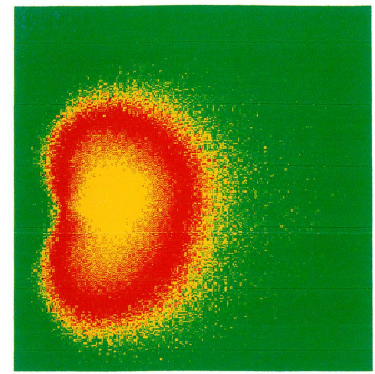
Fig. 5.2a-f. Expansion of the plasma from the target. The positions of the different ion species in the multi-colour images can be seen to the right. A chart of the colour coding is shown above with intensities ranging from 0 pixels (blue) to 255 pixels (white).



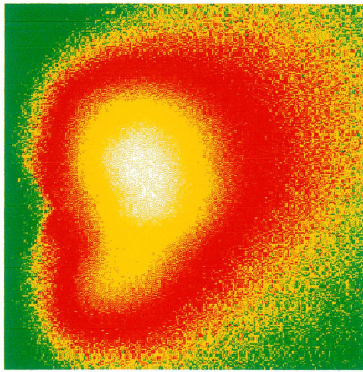
5 mm
a) $t=0$ ns, Amplification = 1.0



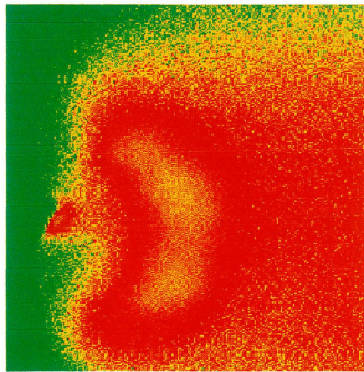
b) $t=25$ ns, Amplification = 2.0



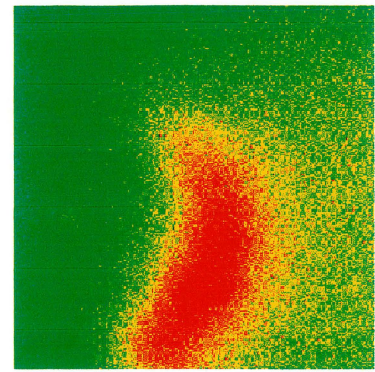
c) $t=75$ ns, Amplification = 4.5



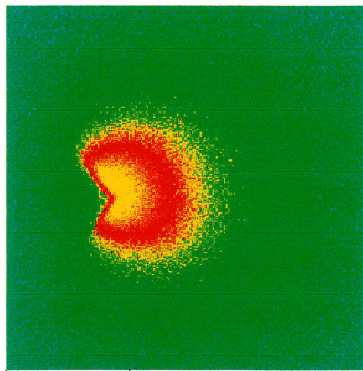
d) $t=125$ ns, Amplification = 10.5
Fig. 5.3a-f. Expansion of CII.



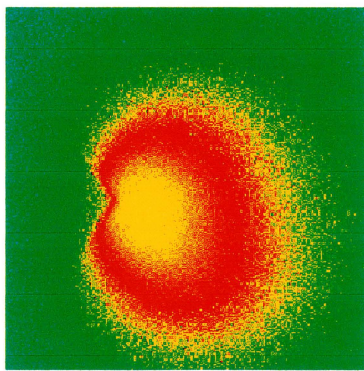
e) $t=175$ ns, Amplification = 13.5



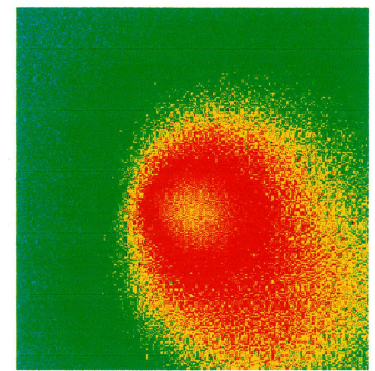
f) $t=225$ ns, Amplification = 13.5



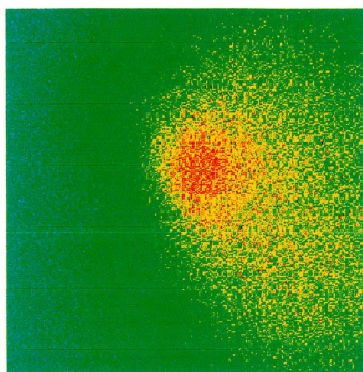
5 mm
a) $t=0$ ns, Amplification = 1.0



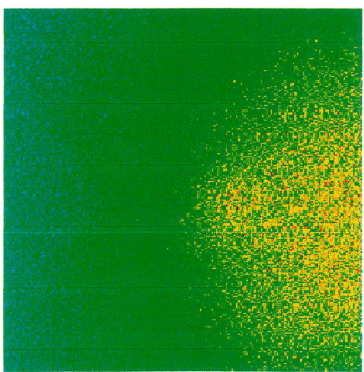
b) $t=25$ ns, Amplification = 2.0



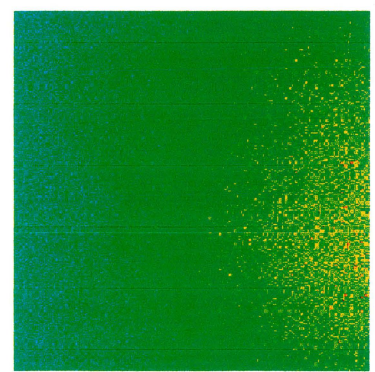
c) $t=50$ ns, Amplification = 3.0



d) $t=75$ ns, Amplification = 3.5
Fig. 5.4a-f. Expansion of CIII.



e) $t=100$ ns, Amplification = 6.0



f) $t=125$ ns, Amplification = 6.0

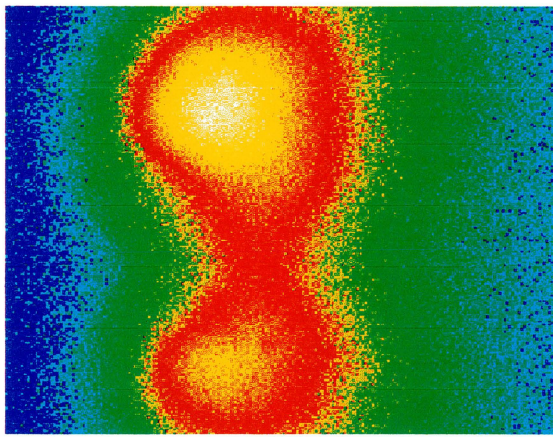
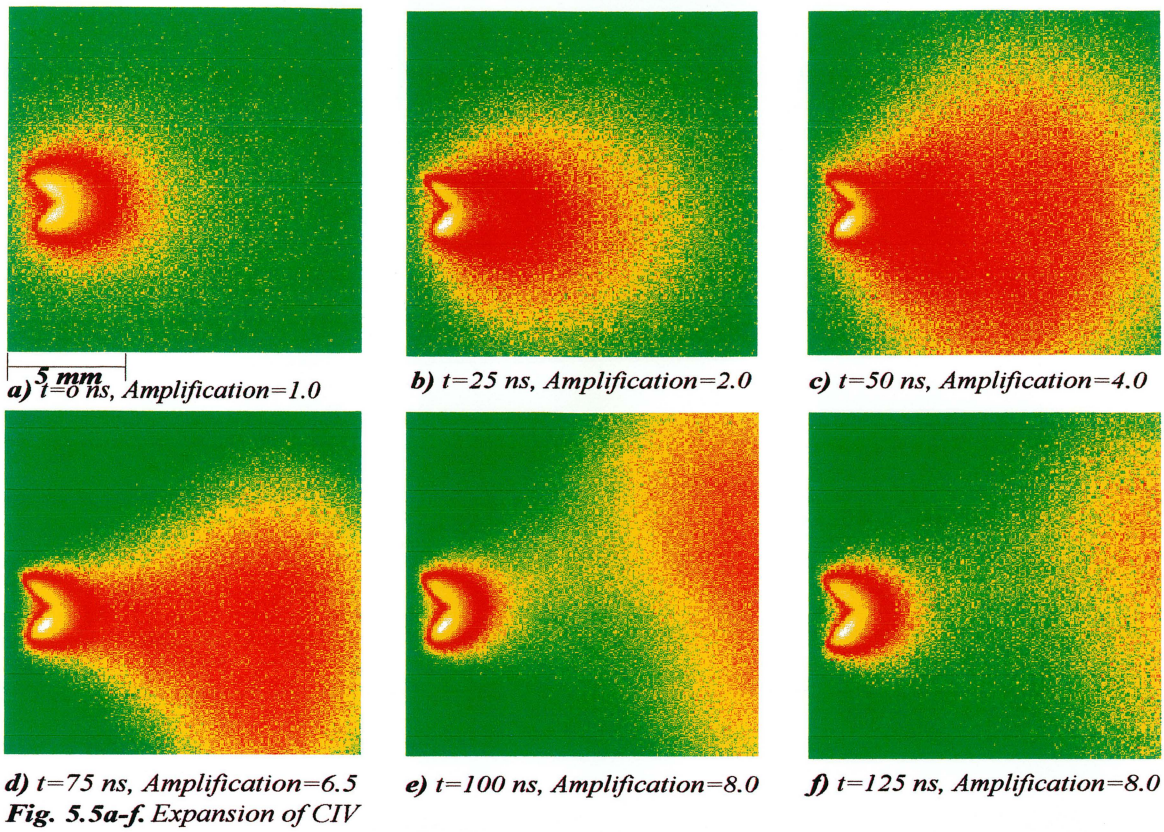


Fig. 5.6. Single colour image of CII where laser beam hits a deep track (not to scale).

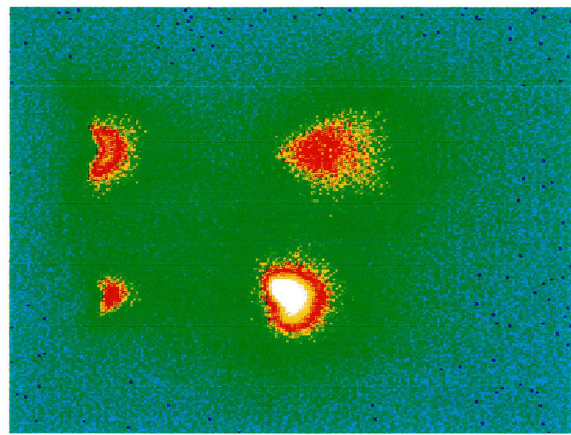
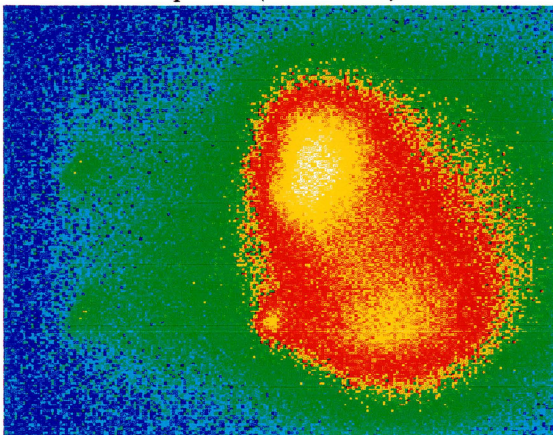
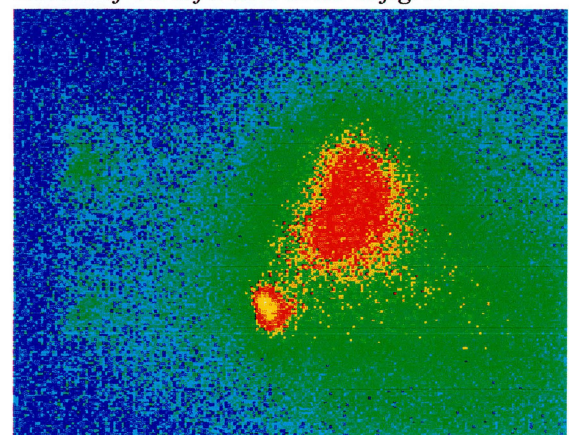


Fig. 5.8. $t=75$ ns. Low irradiance. A small amount of CII is formed. Scale as fig. 5.7.



a) $t=100$ ns



b) $t=175$ ns

Fig. 5.7a-b. Multi-colour images with the Cassegrainian telescope moved further back.

5.2 Spectroscopic studies of the plasma

Using the set-up described in Section 4.2, with the monochromator kept at a constant wavelength, time-resolved studies were done. Four different spectral lines were studied, each representing a species of the ions, at seven distances, z , from the target ($z=1, 5, 10, 15, 20, 25$ and 30 mm). The wavelengths used were CI: 538 nm, CII: 427 nm, CIII: 465 nm and CIV: 581 nm. Typical oscilloscope recordings of CIV are shown in Fig. 5.9 below.

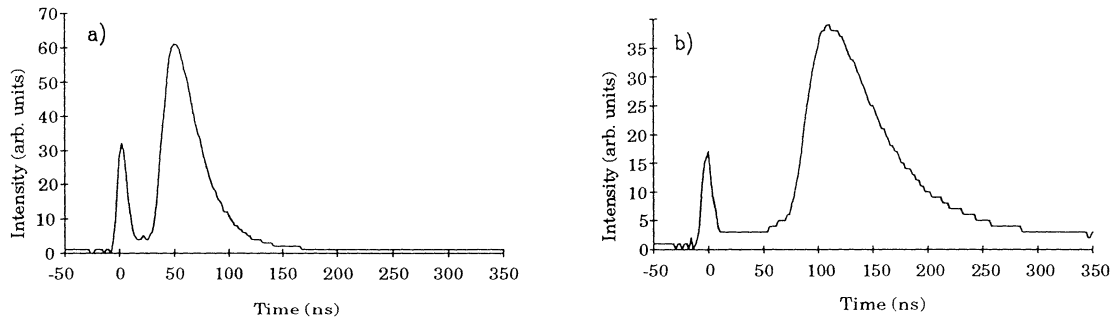


Fig. 5.9a-b. Oscilloscope trace of CIV at a) $z=10$ mm and b) $z=30$ mm.

The figures show the time dependence of line intensities emitted from a small part of the plasma at 10 mm and 30 mm from the target. The first peak is due to the spark, which emits continuous radiation. Ideally, this peak should only exist very close to the target surface. However, due to light scattering, it also appears on the time profiles further away from the target. The second peak shows the time profile of the ion species under investigation. As expected the distance between the two peaks increases further away from the target, since the time between the plasma formation and ion observation is longer. The relative intensities of the two peaks change with increasing target distance, the emission from the spark becoming more dominant close to the target.

The intensities emitted by the different ions at $z=5, 10, 15, 20$ and 30 mm are shown in Fig. 5.10a-d. The generation of the spark is used as a time reference and is put to zero on the time axis. The intensity of each species is scaled to unity at $z=5$ mm. At this distance the most highly ionized ion, CIV, is the first to reach its maximum (at 28ns), followed by CIII (34ns) and CII (at 38ns). The slowest one is CI (at 42ns). With increasing target distance the duration of each ion species increases. This can be understood from the broadening of the peaks.

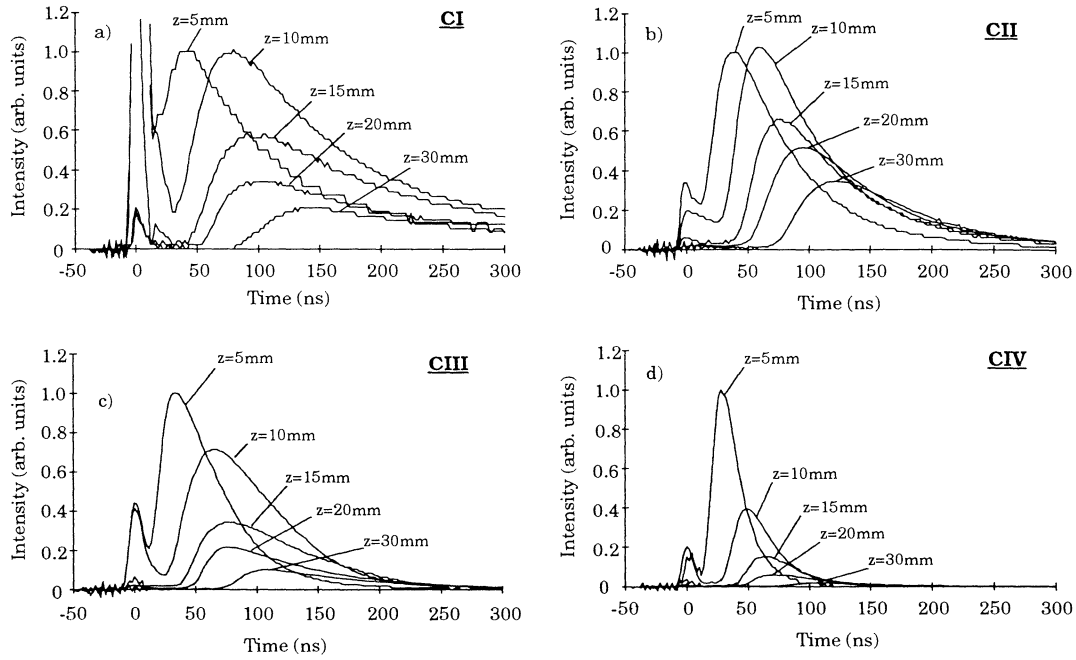


Fig. 5.10a-d. Time dependence of the line intensities emitted by the different ion species.

The variation of the peak intensity as a function of the target distance is shown in Fig. 5.11. Scaling of the intensities has been done by setting the intensity equal to unity at $z=1$ mm. CI has not been included here, since its spectral line is very weak. Close to the target its intensity profile is dominated by the continuous emission from the spark, making the measurement of the maximum intensity unreliable at $z=1$ mm. The figure shows how the maximum intensity decreases further away from the target. This is partially due to the expansion of the plasma and partially due to recombination. The intensity of CIV decreases the fastest, followed by CIII and CII. From the images shown in Fig. 5.3-5.5 it is clear that the higher ion species have a smaller spread as they expand. It would therefore be expected that the intensity decreases faster for low ionization stages. Since this is not the case here, we have interpreted the results to show that the recombination rates are the highest for CIV followed by CIII and CII, respectively.

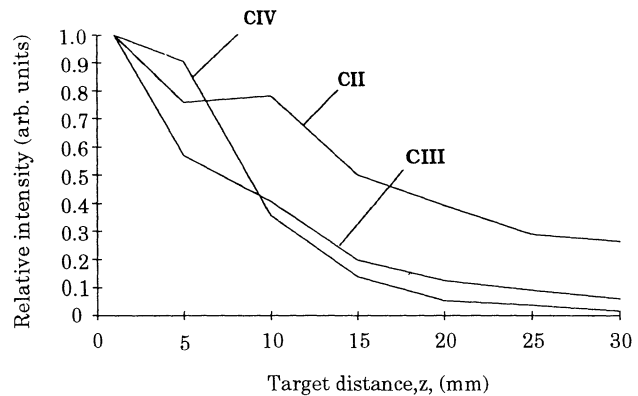


Fig. 5.11. Comparison of the decrease in intensity between the different ion species.

By plotting the distance to the target as a function of the time of the maximum intensity we can estimate the ion velocity. This is done in Fig. 5.12a-d.

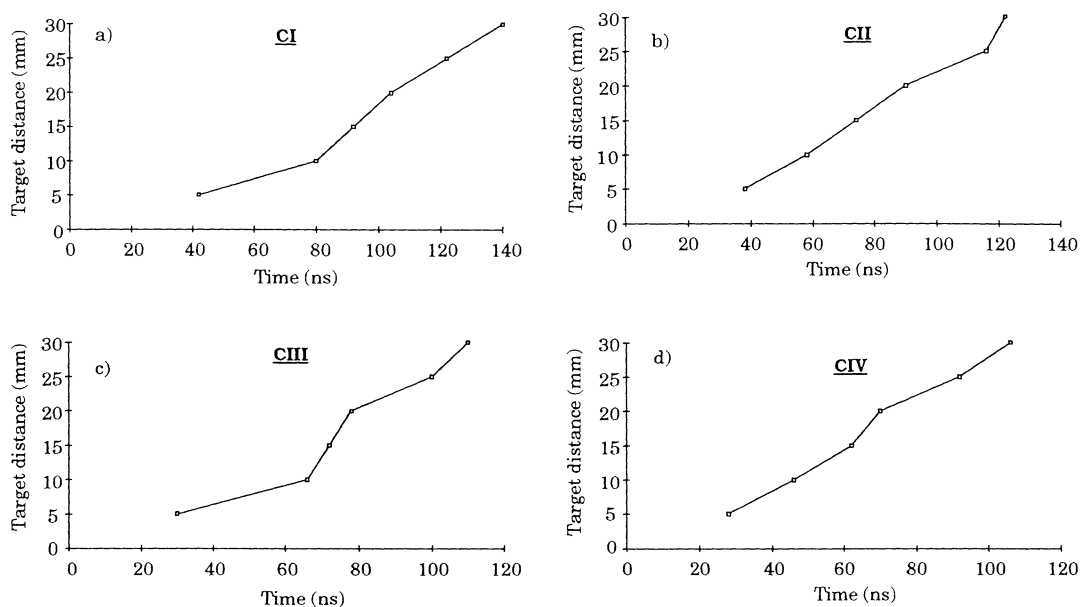


Fig. 5.12a-d. Target distance as a function of the time of maximum intensity for the different ions.

Straight lines approximate the ion velocities and the values in Table 5.2 are obtained.

Line	Ion velocity (cm/s)
CI-538nm	$2.5 \cdot 10^7$
CII-426nm	$2.9 \cdot 10^7$
CIII-465nm	$3.0 \cdot 10^7$
CIV-581nm	$3.3 \cdot 10^7$

Table 5.2. Calculated ion velocities.

5.3 Calculation of electron temperatures

As described in Section 3.2 the population densities of the ground state ions or atoms of charge z , can be related to the population densities of ions of charge $(z+1)$, by Saha's equation (Eq. 3.3). This equation is valid provided the plasma is in LTE. From this equation an expression for the intensity of a spectral line can be derived [17,18]:

$$I = \left(\frac{h^2}{2\pi m_e k T_e} \right)^{3/2} \frac{(g_p)_z A h \nu}{2(g_0)_{z+1} 4\pi} n_e n_{ion,z+1} \exp\left(\frac{\chi_z}{k T_e}\right) * \text{plasma depth} \quad (5.1)$$

The plasma depth is the distance between two points, on either side of the incoming laser light, where the intensity is half of the maximum intensity. A is the transition probability. Values from *Atomic Transition Probabilities* [19] have been used. The statistical weight of the upper energy state of the transition is denoted by $(g_p)_z$. The electron temperature can be calculated by comparing the intensity of two spectral lines from the same ion. However, for Eq. 5.1 to be valid the upper energy state (p) of the transition has to be in LTE with the ground state of the next ion. The LTE model assumes that collisional excitation and de-excitation dominate over radiative processes, and therefore determine the population distribution. If this condition is fulfilled each small volume of plasma will obey the Boltzmann distribution for the energy states within one ion, and the Saha equation for the relative populations among the ionization stages. Hence the name local thermal equilibrium arises. This requires that the electron density satisfies the following relation [9]:

$$n_e \geq 1.73 * 10^{14} T_e^{1/2} \chi(p,q)^3 \quad (5.2)$$

Both T_e and $\chi(p,q)$ are in eV, and n_e is in cm^{-3} . $\chi(p,q)$ is the energy gap between the upper state (p) and the lower state (q) between which the transition occurs. It is reasonable that the higher bound states should be in LTE with the free electrons since these states, besides being coupled to each other by collisional excitation and de-excitation, are coupled to the free electrons by collisional ionization and three-body recombination [20].

Assuming that the LTE model is valid, the electron temperature can be determined with the spectra obtained using the experimental arrangement described in Section 4.2. This was done using two spectral lines from CII, $\lambda_1=426.7$ nm and $\lambda_2=589.1$ nm. Using Eq. 5.2, the ratio between the intensities can be written:

$$\frac{I_1}{I_2} = \frac{q_1 (g_{p_1})_z A_1 \lambda_2}{q_2 (g_{p_2})_z A_2 \lambda_1} \exp\left(\frac{\chi_1 - \chi_2}{k T_e}\right) \quad (5.3)$$

This expression can be used for the determination of the electron temperature. The quantum efficiency of the detector (q), but not the spectral transmission of the lens system, has been taken into account. The following values were taken from *Atomic*

Transition Probabilities [19]: $(g_{p1})=14$, $(g_{p2})=6$, $A_1=2.46*10^8 \text{ s}^{-1}$, $A_2=0.337*10^8 \text{ s}^{-1}$, $\chi_1=3.432 \text{ eV}$ and $\chi_2=4.232 \text{ eV}$. The quantum efficiency was $q_1=0.25$ and $q_2=0.025$.

Using the spectra in Appendix B, the electron temperatures in Table 5.2 below were calculated.

Target distance (mm)	Time (ns)	Electron temperature (eV)
3	50	0.94
3	150	0.55
10	50	0.80
10	400	1.0
20	100	0.61

Table 5.2. Calculated electron temperatures at different times and target distances.

It should be emphasised that the values for the electron temperatures are only valid provided the LTE model can be used. In our case, with $\chi(p,q)\sim 3\text{eV}$ and $T_e\sim 1\text{eV}$, the condition on the electron density becomes $n_e\geq 10^{15}\text{cm}^{-3}$.

Close to the target, at a distance equal to the radius of the focal spot ($r_f\sim 0.05\text{mm}$), the maximum electron temperature is achieved (see Section 3.5). According to Eq. 3.5, with our conditions, $T_{e,\text{max}}$ is in the order of 200 keV.

5.4 Conclusion

A laser-produced carbon plasma has been studied in this diploma thesis. Two-dimensional images were obtained using a multi-colour imaging system and spectral studies were done with the use of a monochromator. Shapes, ion velocities and time of appearance have been studied for the different ions. The results show that the higher ion species have a smaller spread as they expand, a higher ion velocity and appear earlier than the less ionized species. Despite these differences the different ions are not very well separated spatially and temporally. The study included the ions CII, CIII and CIV. Studies of CI used a very weak line. Therefore this ion has only been included where the results are reliable. Electron temperatures in different parts of the plasma have been calculated. However, these are only correct provided that the LTE model is applicable.

Acknowledgements

First, I would like to thank my supervisor Dr. Jörgen Larsson for all the help he has given me with this project. His advice on both theoretical and practical aspects has been invaluable.

I also wish to thank Prof. Sune Svanberg, who with his enthusiastic lectures initiated my interest in this field.

I am grateful to Anders Persson for his help regarding computers.

I would also like to thank my parents for their language corrections.

Finally, I thank everybody at the Department of Atomic Physics. I am very grateful for the support and help I have received.

References

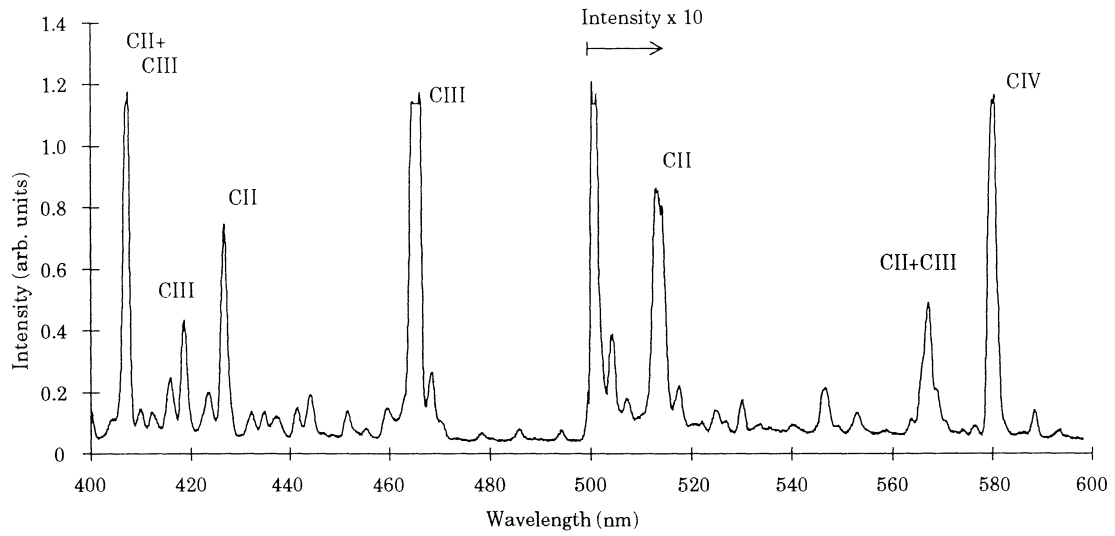
1. R.A. Lacy, A.C. Nilsson, R.L. Byer, W.T. Silfvast, O.R. Wood II and S. Svanberg, *Photoionization-Pumped Gain at 185 nm in a Laser-Ablated Indium Plasma*, J. Opt. Soc. Am. B **6**, 1209-1216 (1989).
2. M.L. Bortz and R.H. French, *Optical Reflectivity Measurements Using a Laser Plasma Light Source*, Appl. Phys. Lett. **55**, 1955-1957 (1989).
3. H. Bergström, G.W. Faris, H. Hallstadius, H. Lundberg, A. Persson and C-G. Wahlström, *Radiative Lifetime and Hyperfine-Structure Studies on Laser-Evaporated Boron*, Z. Phys. D **8**, 17-23 (1988).
4. S.G. Johansson, A. Joueizadeh, U. Litzen, J. Larsson, A. Persson, C- G. Wahlström, S. Svanberg, D.S. Leckrone and G.M. Wahlgren, *Comparison of New Experimental and Astrophysical f -values for some Ru II lines, Observed in HST spectra of χ Lupi*, The Astrophysical Journal, **421**, 809-815 (1994).
5. C-G. Wahlström, S. Borgström, J. Larsson and S-G. Pettersson, *High-order Harmonic Generation in Laser-produced Ions Using a Near-infrared Laser*, Submitted to Phys. Rev. A. (1994).
6. R.A. Lacy, *Gain at 185 nm in a Laser-produced Photoionization-pumped Indium Plasma*, (Stanford University, 1987).
7. T.P. Hughes, *Plasmas and Laser Light*, (Hilger, Bristol, 1975).
8. K. Nishikawa and M. Wakatani, *Plasma Physics*, (Springer-Verlag, Berlin, Heidelberg, 1990).
9. R.W.P. McWhirter, *Plasma Diagnostic Techniques* (ed. R.H. Huddleston and S.L. Leonard), pp.201-64. New York, Academic (1965).
10. D.R. Bates et al. (1962a), *Recombination Between Electrons and Atomic Ions I. Optically thin plasmas*, Proc. Roy. Soc. **A267**, 297-312 (1962).
11. D.R. Bates et al. (1962b), *Recombination Between Electrons and Atomic Ions II. Optically thin plasmas*, Proc.Roy.Soc. **A270**, 156-672 (1962).
12. P.K. Carrol and E.T. Kennedy, *Laser Produced Plasmas*, Contemp. Phys. **22**, 61-96 (1981).
13. H. Puell, *Heating of Laser Produced Plasmas Generated at Plane Solid Targets*, Z, Naturforsch. **25A**, 1807-15 (1970).

14. S. Andersson-Engels, J. Johansson and S. Svanberg, *Multicolour Fluorescence imaging system for tissue diagnostics*, SPIE Proceedings **1205** (1990).
15. P.S. Andersson, S. Montán and S. Svanberg, *Multispectral System for Fluorescence Imaging*, IEEE Journal of Quantum Electronics **23** (1987).
16. P. Kauranen, S. Andersson-Engels and S. Svanberg, *Spatial Mapping of Flame Radical Emission Using a Spectroscopic Multi-Colour Imaging System*, Appl. Phys. **B53**, 260-264 (1991).
17. B.C. Boland, F.E. Irons and P.W.P. McWhirter, *A Spectroscopic Study of the Plasma Generated by a Laser from Polyethylene*, J. Phys. B. **1**, 1180-91 (1968).
18. F.E. Irons, *Stark Broadening of High Quantum Number $\Delta n=1$ Transitions of Carbon V and VI in a Laser-produced Plasma*, J. Phys. B. **6**, 1562-1581 (1973).
19. W.L. Wiese, M.W. Smith and B.M. Glennon, *Atomic Transition Probabilities*, National Bureau of Standards 4 (1966).
20. F.E. Irons and N.J. Peacock, *A Spectroscopic Study of the Recombination of C^{6+} to C^{5+} in an Expanding Laser-produced Plasma*, J. Phys. B. **7**, 2084-2099 (1974).

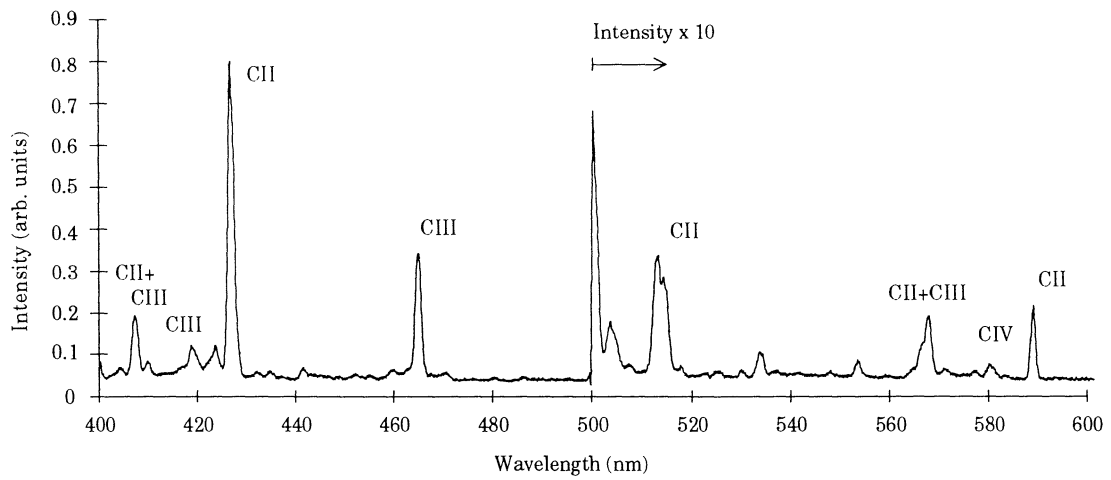
Appendix A - Table of carbon spectral lines

<u>Wavelength</u> <u>(nm)</u>	<u>Ion</u>	<u>Intensity</u> <u>(arb. units)</u>
405.721	C III	150
406.909	C III	200
407.006	C III	250
407.141	C III	250
407.567	C II	250
407.700	C II	350
416.403	C III	150
418.808	C III	250
426.820	C II	800
426.846	C II	1000
432.678	C III	200
464.872	C III	600
465.155	C III	520
465.277	C III	375
465.960	C IV	200
466.717	C III	200
477.308	C I	200
493.343	C I	200
494.526	C V	5
494.594	C V	5
505.358	C I	200
513.437	C II	350
513.471	C II	350
514.492	C II	350
514.659	C II	570
515.252	C II	400
538.184	C I	300
564.964	C II	250
566.404	C II	350
569.750	C III	450
580.294	C IV	250
581.359	C IV	200
582.804	C III	150
589.140	C II	570
589.322	C II	350
600.279	C I	200
600.769	C I	250
600.884	C I	110

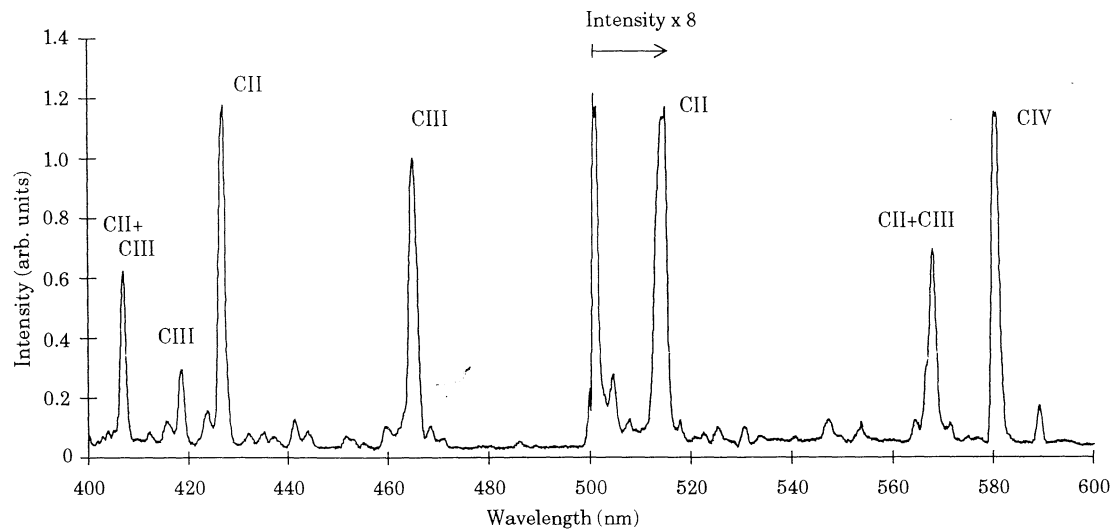
Appendix B - Carbon spectra



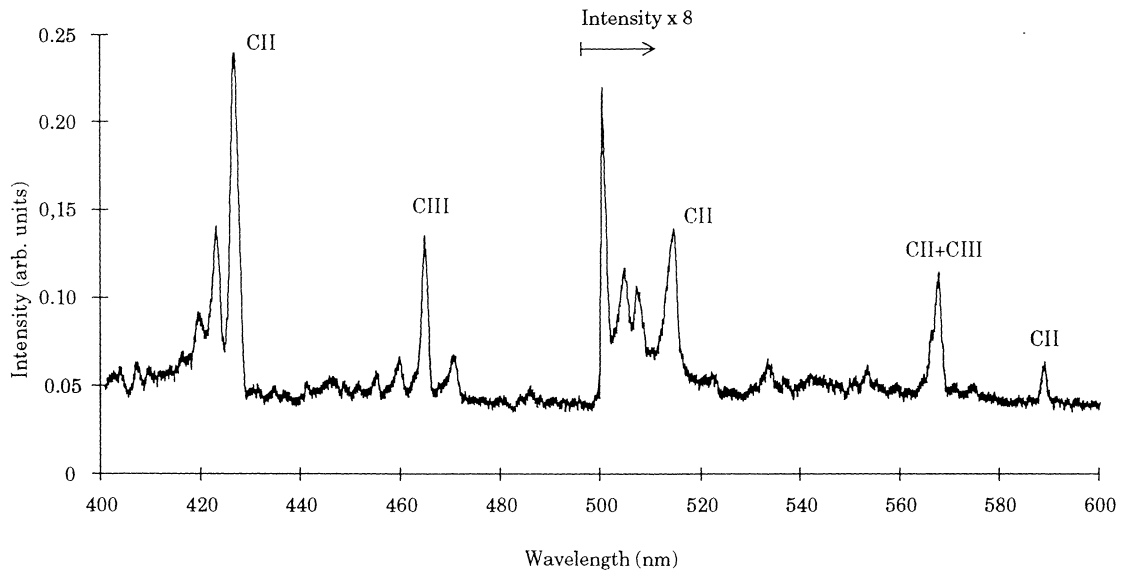
a) z=3 mm, t=50 ns



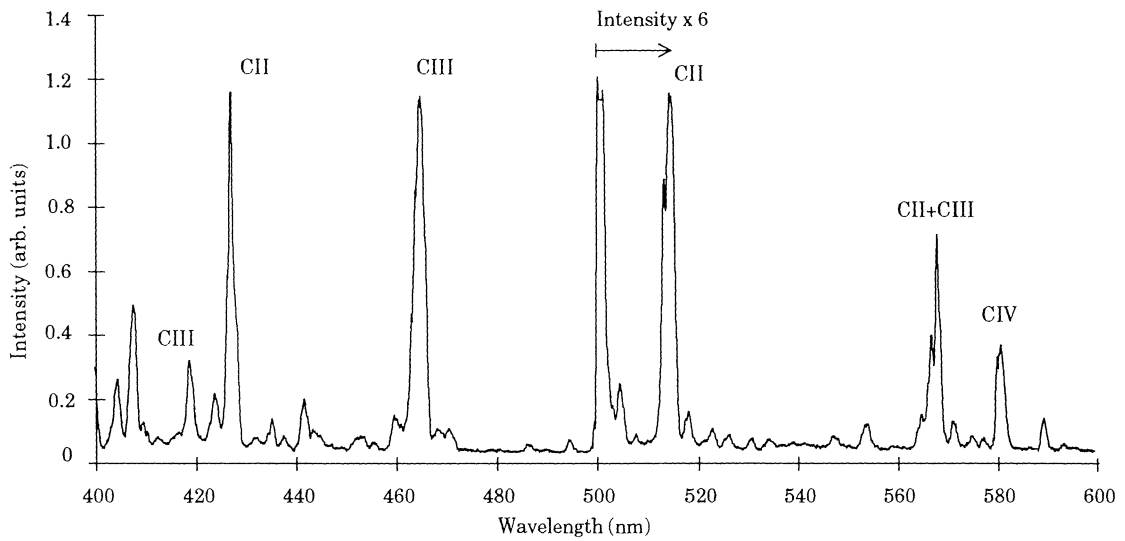
b) z=3 mm, t=150 ns



c) z=10 mm, t=50 ns



d) $z=10\text{mm}$, $t=400\text{ ns}$



e) $z=20\text{ mm}$, $t=100\text{ ns}$

Fig. B1a-e. Carbon spectra at various times and distances from the target.

Spectra used for electron temperature calculations. The voltage over the photomultiplier has been raised at 500 nm, increasing the sensitivity by the factor given in the figures.